ACSNANO

www.acsnano.org

ARTICLE

Atomistic Insights on the Full Operation Cycle of a HfO_2-Based Resistive Random Access Memory Cell from Molecular Dynamics

M. Laura Urquiza, Md Mahbubul Islam, Adri C. T. van Duin, Xavier Cartoixà,* and Alejandro Strachan*

Cite This: *ACS Nano* 2021, 15, 12945−12954

Read Online

ACCESS | Metrics & More | Article Recommendations | Supporting Information

ABSTRACT: We characterize the atomic processes that underlie forming, reset, and set in HfO_2-based resistive random access memory (RRAM) cells through molecular dynamics (MD) simulations, using an extended charge equilibration method to describe external electric fields. By tracking the migration of oxygen ions and the change in coordination of Hf atoms in the dielectric, we characterize the formation and dissolution of conductive filaments (CFs) during the operation of the device with atomic detail. Simulations of the forming process show that the CFs form through an oxygen exchange mechanism, induced by a cascade of oxygen displacements from the oxide to the active electrode, as opposed to aggregation of pre-existing oxygen vacancies. However, the filament breakup is dominated by lateral, rather than vertical (along the filament), motion of vacancies. In addition, depending on the temperature of the system, the reset can be achieved through a redox effect (bipolar switch), where oxygen diffusion is governed by the applied bias, or by a thermochemical process (unipolar switch), where the diffusion is driven by temperature. Unlike forming and similar to reset, the set process involves lateral oxygen atoms as well. This is driven by field localization associated with conductive paths.

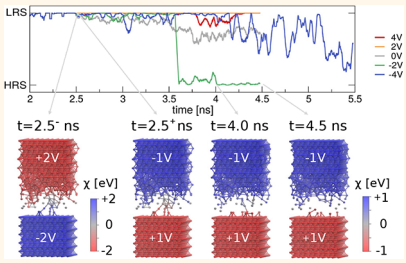

KEYWORDS: *RRAM, valence change mechanism, MD, forming-reset-set, EChemDID*

Resistive random access memories (RRAMs) are considered the most promising candidates for next generation, high-scaling, ultrafast, and low power consumption memories.[1−3] RRAM cells, that typically consist of a metal−insulator−metal (MIM) stack, store bits by reversibly changing the resistivity of the insulator between a high-resistance state (HRS) and a low-resistance state (LRS). In order to enable this reversible change, the devices normally require an initial and irreversible process called electroforming, which is basically a current-controlled breakdown of the pristine highly resistive oxide layer.[4−6]

In most RRAM devices, the switching between LRS/HRS originates from the formation/rupture of a nanoscale conductive filament (CF) in the dielectric layer. This is the case of memories operating through electrochemical metallization mechanism (ECM), where the CF consists of cations of a metal injected from an electrochemically active electrode, which reduce and nucleate forming a filament starting from the cathode or the anode, depending on which of reduction and nucleation or cation transport is the rate-limiting process.[7] Also exhibiting filamentary conduction are cells that operate via the valence change mechanism (VCM); in this case, a variation in local stoichiometry arising from the presence of oxygen vacancies changes the valence of the metallic ions rendering them conductive.[4] It should be noted that, in general, the presence of oxygen vacancies is not a sufficient condition to obtain electronic conduction in an oxide. For example, vacancies in zirconia can be generated by the addition of an oxide with a lower valence cation, such as Y_2O_3, a procedure used to stabilize the cubic phase of zirconia at low temperature while maintaining its electronic insulator character.[8,9] This is, however, not the situation in HfO_2 or ZrO_2 without external impurities, given that Hf_2O_3 and Zr_2O_3 have been predicted to be semi-metallic by first-principles calculations.[10]

This paper focuses on HfO_2-based RRAM devices that operate through the VCM. In the valence change mechanism, the formation and dissolution of the CF is governed by the migration of oxygen anions, driven by an external electric field. The reduction of the oxide in O-depleted areas results in a change in valence of the metallic ions atoms (Hf in our case) which, in turn, is responsible for the electronic conductivity in the LRS.[11,12] The details behind the migration of ions are not

Received: February 17, 2021
Accepted: July 27, 2021
Published: July 30, 2021

https://doi.org/10.1021/acsnano.1c01466
ACS Nano 2021, 15, 12945−12954

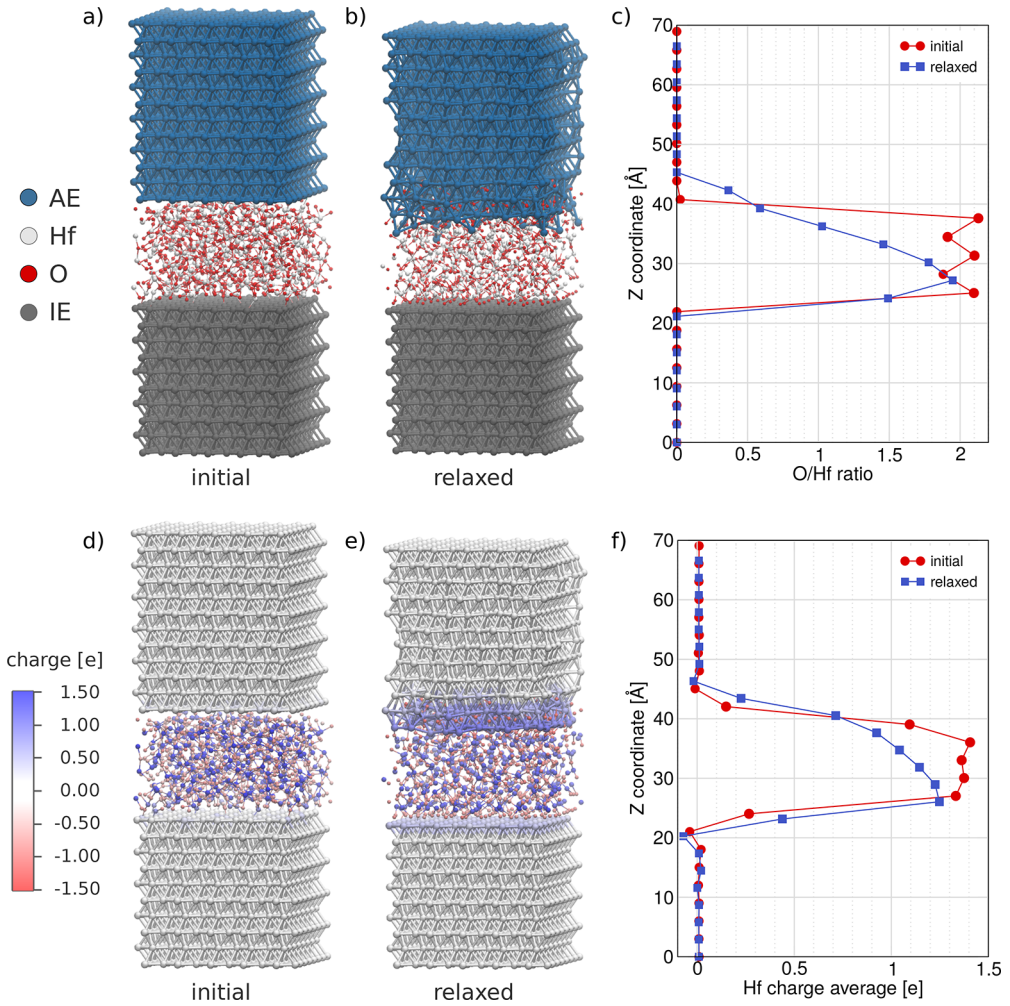

Figure 1. Atomic structure of sample A at (a) the initial state and (b) after the interface relaxation. (c) Stoichiometry profiles of the cell along the *z*-axis at time 0 and 100 ps. (d) Initial and (e) final atomic charges. (f) Hf charge profile along the *z*-coordinate for the initial and relaxed structures. The snapshots were generated with VMD software.[22,23]

known, and the nanoscale size of the devices compounded with ultrafast switching makes the experimental characterization of these processes extremely difficult. In this paper, molecular dynamics simulations reveal the atomic level processes associated with the forming, reset, and set processes.

Depending on the choice of electrode materials, the devices can be operated in unipolar or bipolar switching modes. For a bipolar behavior, metals with high oxygen affinity are chosen as the active electrode (AE), whereas inert metals are preferred for the inactive electrode (IE). The AE plays an important role in the operation of VCM cells because it acts as an oxygen exchange layer, creating a substoichiometric region at the oxide interface that contributes significantly to reduce the forming voltage and improve the endurance and retention of the cell.[13−15] The most used AE materials are Ti, Hf, and Ta due to their oxygen scavenging ability and good electrical performance.[14,16]

Despite the significant experimental[17] and theoretical[18] evidence supporting the switching mechanism described above, the nature of this phenomena, operating at the nanoscale and in ultrafast regimes, has precluded the development of a detailed, atomic-level understanding of the formation and rupture of the CF, much less an understanding of the variability in the switching and stability of the CF. Molecular dynamics (MD) simulations are an ideal tool to address these questions as recent developments[19] enable the application of an external electrochemical potential into reactive simulations that track individual atoms. Furthermore, as was demonstrated for ECM cells,[20] the nanoscale dimensions and ultrafast switching characteristics of these devices enable an explicit, all-atom description of their operation.

We report MD simulations of the operation of HfO_2-based RRAM cells that explicitly capture all the relevant processes involved in the switching of the device, including redox reactions, oxygen migration, growth of vacancy-rich regions, and the effect of temperature. These simulations provide a comprehensive dynamical picture of the formation and dissolution of the CF in these devices. We studied cells with metallic Hf as AE, and our simulations reproduce the substoichiometric layer generated at the oxide/AE interface during the fabrication of the devices. A detailed 3D analysis of the motion of O ions during forming, reset, and set processes reveal an unexpected phenomena. During forming, net oxygen migration toward the AE dominates the formation of the CF. Our results support the viewpoint that the filament rupture during reset is governed by lateral oxygen migration, induced by the complex 3D electric fields from the neighboring ions

https://doi.org/10.1021/acsnano.1c01466
ACS Nano 2021, 15, 12945−12954

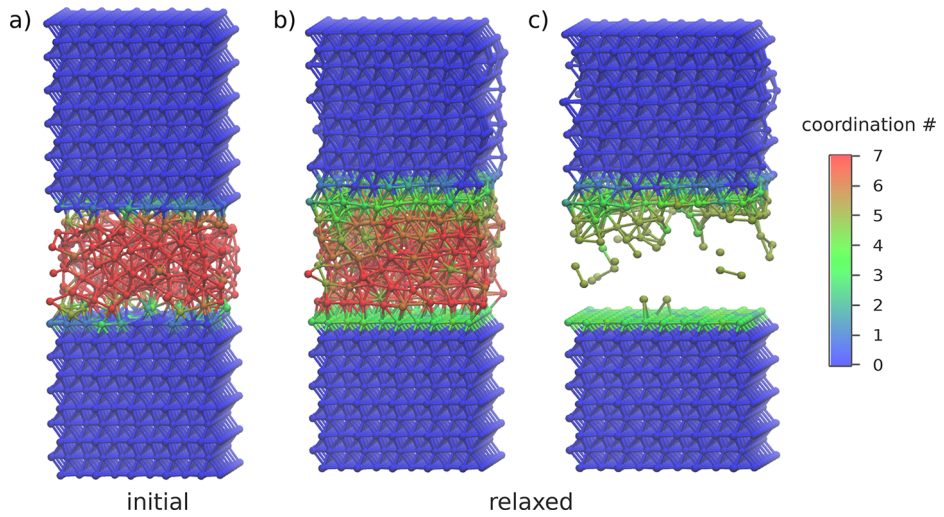

Figure 2. Snapshots of Hf atoms colored according their coordination number for (a) the initial structure, (b) the relaxed structure, and (c) the relaxed structure plotting only under-coordinated Hf atoms. The snapshots were generated with VMD software.[22,23]

and irregular electrode shape during reverse bias in the bipolar case, or by the effect of temperature under unipolar operating conditions. Finally, simulations of the set process demonstrate negligible vertical oxygen migration, in contrast to the forming process, and the filament forms by the rearrangement of oxygen atoms in the lateral directions. This takes place even in absence of large temperature gradients, which are known to favor the set process by the appearance of thermophoretic effects.[21]

RESULTS AND DISCUSSION

Device Structures and Suboxide Formation. As mentioned before, a robust switching in VCM devices requires some amount of oxygen deficiency in the dielectric film. These vacancy profiles can be generated by an electrode that partially oxidizes[12,13,16] or by other methods.[15,24] In our simulations, the relaxation of the HfO_2/Hf interface naturally leads to the generation of a suboxide layer and a high concentration of vacancies in the initially stoichiometric dielectric. The equilibration is carried out at T = 300 K and P = 1 atm for 100 ps to generate a fully relaxed HfO_2/Hf interface. The time considered is enough to ensure that further oxygen migration toward the AE be negligible. In our samples, the diffusion of oxygen atoms toward the AE increases the thickness of the oxide layer by approximately 0.5 nm. Although there are no experimental data for the thickness of the interlayer formed between Hf and HfO_2, our result is similar to the 1.3 nm obtained via XRD for the TiOx layer at a HfO_2/Ti interface.[25] This provides an important, if indirect, validation of our approach.

Figure 1a,b shows snapshots of the initial and relaxed structures of one of the samples generated through melt/quench process (sample A). Figure 1c plots the planar average of the O/Hf atomic number ratio (stoichiometry) along z for the two states. Here, it can be seen that the initial stoichiometry, corresponding to HfO_2 evolves to a profile HfO_x, with x ranging from 2 at the IE interface, to 0.5 at the AE interface. In the Supporting Information we display the same plots for the five different samples generated, obtaining similar results for all cases.

Figure 1d,e show the atomic charges corresponding to same initial and final structures mentioned above, and Figure 1f displays the planar average of the hafnium charge along the z-coordinate. The figures demonstrate how self-consistent charge equilibration results in neutral electrodes and positively charged Hf ions in the oxide and suboxide layers. The atomic charge evolution of the Hf atoms after the relaxation provides clear evidence of the oxidation of Hf atoms at the AE and the consequent reduction of amorphous HfO_2 ($aHfO_2$).

The suboxide layer formed as a consequence of the oxidation/reduction process results in a change of the Hf valence. Given the importance of the valence change in Hf ions during the switching of the devices, we characterized it through the oxygen coordination of Hf atoms, as detailed in the "Filament Description" section below. The results are shown in Figure 2a,b with the snapshots corresponding to the initial and fully relaxed state, respectively. In the images, the color code ranges from blue representing Hf atoms with no oxygen neighbors (i.e., 100% metallic hafnium) to red representing Hf atoms with at least 7 oxygen bonds (i.e., fully oxidized). Before relaxation, Hf atoms from the oxide are mostly 7-fold coordinated, as expected for the HfO_2 structure. When the interface relaxation occurs, this value decreases, generating a high concentration of Hf with metallic behavior, mainly at the AE interface. This trend agrees with DFT calculations, which predict that the formation energy of an oxygen vacancy decreases toward the interface, suggesting that it is thermodynamically more favorable to remove an oxygen atom from the interface region than from the bulk region.[26] In Figure 2c, we display only Hf atoms with coordination equal or lower than 5, considered as metallic. The representation of dynamic bonds shows that the interface relaxation does not lead to formation of the CF.

Forming. Simulating the forming process requires the application of an external field between the metallic electrodes. In experiments, the magnitude of the field applied during forming depends on the original amount of oxygen vacancies (i.e., the stoichiometry of the HfO_x layer). For HfO_2/Hf cells, the values are few tens of meV/Å (0.04[16] and 0.06 eV/Å).[11] We simulated the forming process by applying 4 V difference between the electrodes, which corresponds to an external field equivalent to 0.2 eV/Å. The voltage was applied in isochoric, isothermal MD simulations (NVT ensemble) at 300 K,[27,28] following the scheme described in the "Methods" section. The

https://doi.org/10.1021/acsnano.1c01466
ACS Nano 2021, 15, 12945−12954

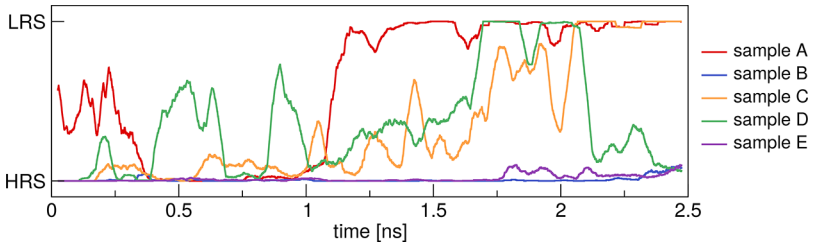

Figure 3. Switching dynamics of the five samples considered, carried out through cluster analysis of conductive Hf atoms, using a cutoff of 3.9 Å. The switching state evolution has been averaged using a moving window of 0.02 ns for clarity.

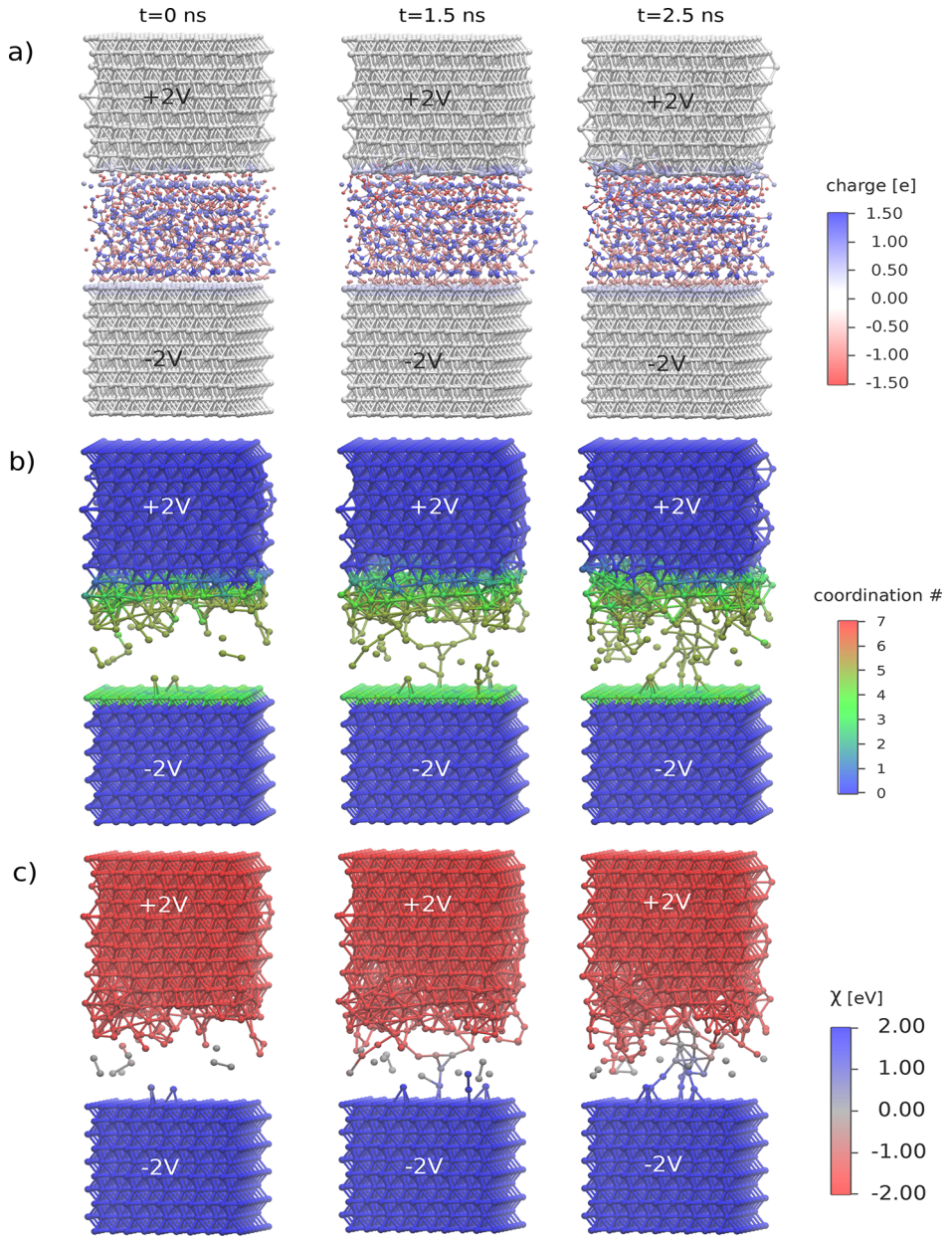

Figure 4. Snapshot of the (a) atomic charges, (b) coordination number of Hf atoms, and (c) potential of Hf atoms, at the beginning (t = 0 ns), just when the filament is fomed (t = 1.5 ns) and at the end of the simulation (t = 2.5 ns). The snapshots were generated with VMD software.[22,23]

voltage chosen was high enough to ensure the formation of the CF occurs within the time scales accessible to MD simulations. The AE was polarized positively, with a potential of +2 V, in order to attract the oxygen atoms, while the IE was set to −2 V. Figure 3 shows that from a total of five independent samples only three switched and two formed a stable filament within the time considered of 2.5 ns. The relatively low probability of switch of the simulated cells is related to the small cross-

https://doi.org/10.1021/acsnano.1c01466
ACS Nano 2021, 15, 12945−12954

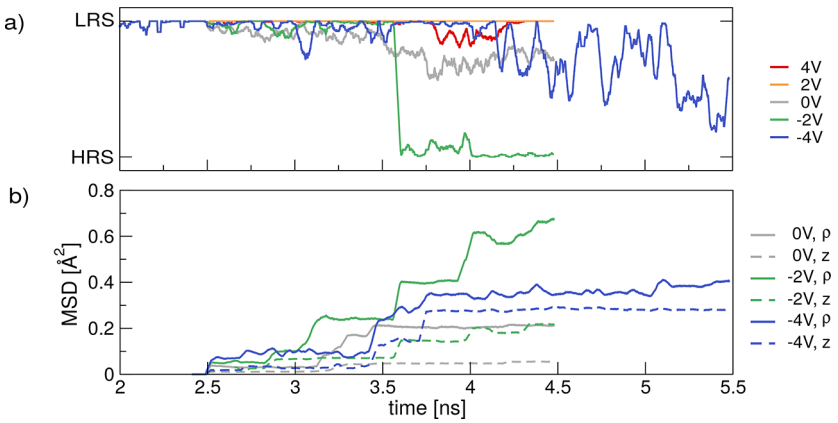

Figure 5. (a) Switching dynamics of sample A under different voltages at 300 K, carried out through cluster analysis of conductive Hf atoms, using a cutoff of 3.9 Å. The switching state evolution has been averaged using a moving window of 50 ps for clarity. The −4 V curve has been extended in order to show more clearly the tendency to break the filament. (b) Mean square displacement (MSD) of oxygen atoms in the filament region (cylinder with radius 5 Å and z between 27 and 40 Å), along the xy-plane (radial coordinate, denoted as ρ) and z-coordinate.

sectional device area and short time scales of the simulations, as detailed in Figure S9.

Figure 4 shows atomic snapshots at various times during the process of forming of sample A. Figure 4a highlights atomic charges and shows that the AE further oxidizes with the applied potential, generating additional oxygen vacancies in the oxide layer. Figure 4b colors atoms by Hf coordination, with a value ≤5 corresponding to the conductive Hf atoms. Figure 4c shows the electronegativity of metallic Hf assigned by EChemDID. Before the forming, EChemDID propagates the electronegativity over the metallic atoms according to their connectivity with the electrodes. When the CF forms, the electronegativity of the metallic ions varies linearly, according to the atomic position between the two electrodes. These plots provides an atomistic picture of the evolution of the CF, that starts as a single-atom chain, just after the switching, and subsequently grows while the potential is kept applied. According to the results, the narrowest constriction is observed near the inactive interface. These findings agree with the quantum point contact model, which states the CF consists of an atomic size chain, or constriction, that behaves as a quantum wire.[29]

Atomistic Mechanisms Behind Forming. In VCM cells, two different forming mechanisms have been proposed in literature over the last years.[30] The first one postulates the generation of anti-Frenkel pairs (an interstitial oxygen O_i and an oxygen vacancy V_O) when an external electric field is applied, followed by the migration of the interstitial oxygen toward the AE. In this model, oxygen vacancies are assumed to be immobile, providing conduction by trap-assisted tunneling. The other mechanism postulates the vacancies are generated as result of an oxygen exchange reaction at the anode (AE), followed by the migration of the oxygen vacancy to the cathode (IE). In this case, the vacancy migration occurs through successive oxygen exchanges between the empty space generated by the reaction with the AE and the adjacent oxygen atoms.

MD simulations carried out on cubic and monoclinic HfO_2 have demonstrated that anti-Frenkel pair generation/recombination is not possible in crystalline structures due to the considerably high electric field required to create O_i−V_O pairs (only sporadic defects are generated at 0.3 eV/Å) and short recombination times (1−4 ps) .[31] This, plus some additional general considerations regarding the observation of reproducible switching in electro-forming-free substoichiometric HfO_2,[24] have led Menzel and Waser to conclude that a switching mechanism based on anti-Frenkel pair generation/recombination cannot take place in HfO_2.[30]

We analyzed the forming mechanism by plotting the migration of oxygen atoms as a function of time for two different kind of simulations: In one case, the electronegativity was updated periodically as described in the "Methods" section, and in the other case, the electronegativity was modified only in 100% metallic Hf at the beginning and maintained as fixed during the rest of the simulation. The aim of this last procedure is to maintain fixed the AE/HfO_2 interface during the forming process. The migration profiles for both cases are displayed in Figure S6. For simulations with the electronegativity fixed, the plots display abrupt oxygen displacements that start at the upper oxygen layer and are followed by displacements of the subsequent layers. Visual inspection of the trajectories shows that each abrupt displacement in the upper oxygen layers corresponds to a large displacement in z of a single oxygen atom. This result demonstrates that oxygen atoms from the first layer that diffuse toward the AE leave behind empty spaces that are occupied by oxygen atoms from the second layer, producing in this way a cascade of displacements that attenuate as the distance to interface increases. For the case where the electronegativity updates during the simulation, the results are quite similar. However, since there are Hf atoms from the oxide that become metallic as the filament evolves, the potential propagates inside the oxide, favoring the oxygen migration in the deeper layers. Our results are a clear evidence that the forming mechanism operating in amorphous HfO_2 is the oxygen exchange across AE/HfO_2 interface.

Reset Process. To understand the nature of the reset mechanism, we ran simulations under different voltages and temperatures. We used sample A for the studies since this is the MIM structure that demonstrated the strongest switch. The switching behavior under different voltages at 300 K is presented in Figure 5a. The results show that the filament remains stable as long as the forming polarity is maintained (i.e., positive potential in the AE and negative potential in the IE). When the voltage is removed, the filament destabilizes and, finally, it dissolves when the polarity is reversed, indicating

https://doi.org/10.1021/acsnano.1c01466
ACS Nano 2021, 15, 12945−12954

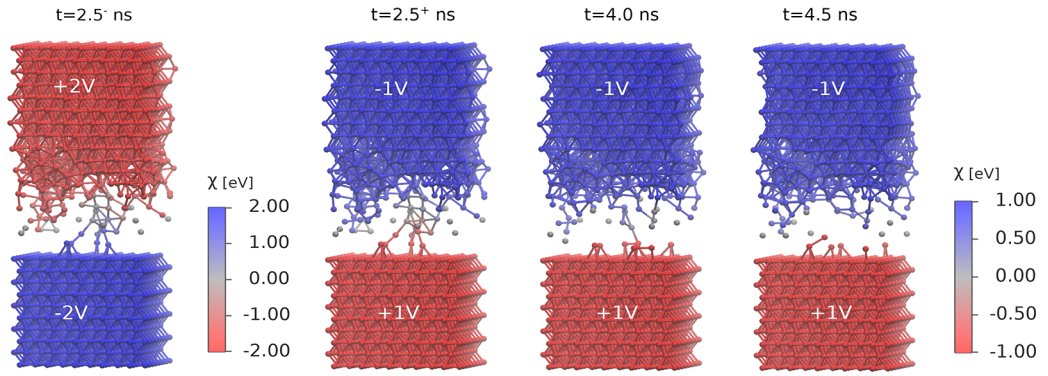

Figure 6. Snapshot of the reset process colored by potential of Hf atoms for different times. The snapshots were generated with VMD software.[22,23]

a clear bipolar behavior. The oxygen migration profiles in Figure S7 demonstrate that the motion of oxygen atoms along the field direction at 300 K is almost negligible; only simulations with voltages of +4 V (−4 V) showed small displacements toward the AE (IE). These results indicate that the oxidation produced during the forming process is irreversible, and the filament rupture must occur by a reorganization of the oxygen atoms in the *xy*-plane. Figure 5b) displays the lateral and *z* mean square displacement (MSD) of the oxygen atoms in the filament region (a cylinder with a radius of 5 Å and *z* between 27 and 40 Å), showing a strong correlation with the filament stability. On the basis of the snapshots of Figure 6, we infer that the driving force for the localized *xy* oxygen migration is the positive potential (negative electronegativity) propagated over the filament, inducing a local oxidation.

When the system temperature is increased to 400 K, the filament destabilizes and breaks in all cases, as shown in Figure 7. This is true even when applying a bias with the same polarity

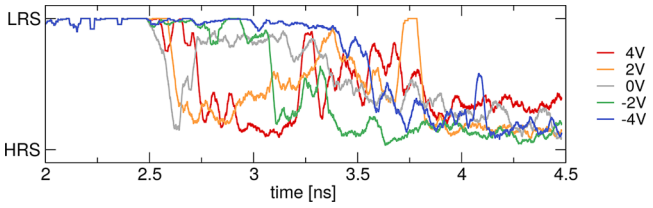

Figure 7. Switching dynamics of sample A under different voltages at 400 K, carried out through cluster analysis of conductive Hf atoms, using a cutoff of 3.9 Å. The switching state evolution has been averaged using a moving window of 0.05 ns for clarity.

as the forming process, which induces a small additional oxygen migration toward the AE (Figure S7) that, in principle, would favor filament stability. This is because increasing the temperature of the system favors diffusion, not only along the field direction, but also in the *xy*-plane, which is the main cause of the filament dissolution, as observed previously for samples at 300 K.

Our findings are in agreement with experiments where the current compliance is released during reset to produce the filament rupture by Joule heating,[4] suggesting that reset in bipolar HfO_2-based cells can also be induced by thermal activation. Similar results where observed in bipolar TiO_2-based RRAM cells, where by setting a large compliance current value, the cell turned to unipolar switching.[32]

Set Process. The set process was simulated by reversing the polarity of the external field for a second time. In this case, we applied 4 V between the metallic electrodes to ensure that the filament formation occurred within the time accessible to the simulations. Since the characteristic time for oxygen hops within the oxide is relatively slow (~0.5 ns), we slightly increased the temperature (up to 325 K) in order to accelerate the process. We used the MIM structure obtained after the bipolar reset at −2 V and 300 K, which demonstrated a complete dissolution of the conductive filament. The results are shown in Figure 8, where we observe that the filament starts forming after 0.5 ns, and it remains stable during the rest of the simulation. Again, the process occurs with a significant contribution by the reorganization of oxygen atoms in the *xy*-plane, which leads to a new filament. We also see that no set event occurs when the applied bias is 0 or −4 V.

The resulting filament at 4 V (Figure 9) differs from the initial one, obtained after the forming process. However, since the area of the device considered here is relatively small, this finding is not indicative that the filament might form in a different region during the successive set.

CONCLUSIONS

In summary, we presented atomic simulations of the forming, reset, and set processes in HfO_x-based MIM devices. We generated substoichiometric HfO_x profiles consistent with those obtained experimentally during the fabrication of RRAM cells by relaxing hafnium/hafnia interfaces. The relaxed samples were used to simulate the forming, reset, and set processes under operating conditions. To simulate the application of external electrochemical potentials in the metallic electrodes, we generalized the EChemDID method for valence change systems. This method, combined with reactive MD simulations, enabled the atomic-level description of the redox and transport processes responsible for resistance switching.

The dynamics associated with the change in valence, responsible for resistance switching, was characterized on the fly by tracking the correlated motion of O ions and change in O-coordination of the Hf atoms. With this approach, we identified the formation and rupture of an atomic conductive filament. The simulations revealed the atomistic mechanism for the forming process in nanoscaled cells, consisting in a cascade of oxygen displacements initialized at the interface, similar to the oxygen exchange mechanism previously proposed based on experiments. We also found that under the model assumptions and the considered filament size the

https://doi.org/10.1021/acsnano.1c01466
ACS Nano 2021, 15, 12945−12954

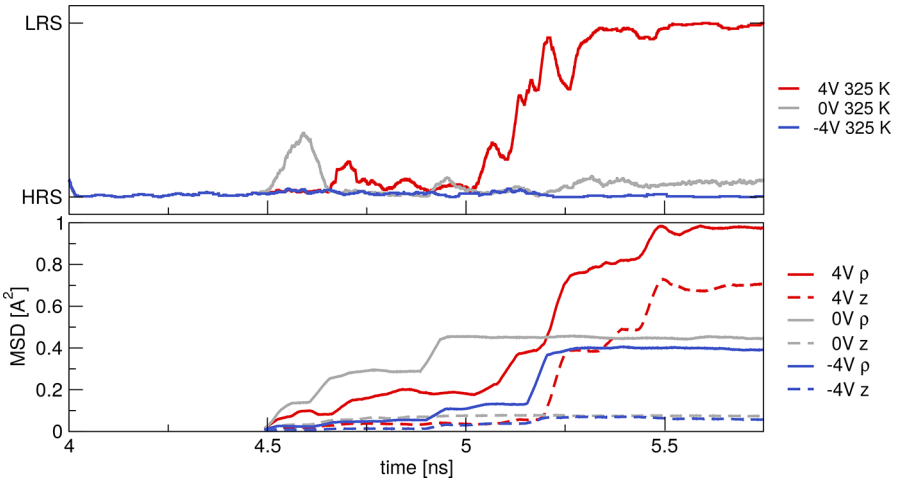

Figure 8. (a) Switching dynamics of the set simulation for several applied bias at 325 K. The structure corresponds to sample A after reset at 2 V and 300 K. See the caption of Figure 5 for the description of how we obtained the switch curve. (b) MSD of oxygen atoms near the filament, inside a cylinder with radius 5 Å and *z* between 27 and 40 Å, along the radial and *z*-coordinate.

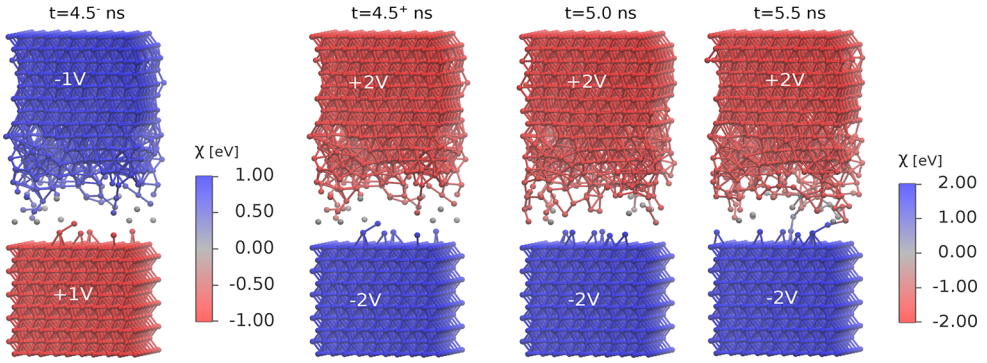

Figure 9. Snapshot of the set process colored by potential of Hf atoms for different times. The snapshots were generated with VMD software.[22,23]

reset and set processes occur through a local reorganization of oxygen atoms in the filament region; these processes are dominated by lateral oxygen migration with minimal motion toward the AE or IE. These insights into the switching mechanisms behind nanoscale HfO_2-based RRAM devices could enable further materials optimization efforts and the assessment of ultimate scalability of this technology.

METHODS

Atomistic Device Model. The simulated RRAM cells consist of an amorphous HfO_2 ($aHfO_2$) layer sandwiched between an AE and an IE. We use Hf as the AE as it is widely used experimentally to induce the formation of a substoichiometric HfO_x layer at the HfO_2/Hf interface. To simplify the simulations, the IE is also described by Hf atoms, but the positions of these atoms are fixed throughout the simulation rendering them inactive. The initial simulation box consist of a 10 × 8 × 6 hcp-Hf supercell with 960 atoms in the AE, an $aHfO_2$ supercell containing 900 atoms, and a 10 × 8 × 5 hcp-Hf supercell in the IE with 800 atoms.

To consider the natural device-to-device variability of the real cells, five different $aHfO_2$ structures were generated through a melt/quench process and attached to metallic electrodes. The melt of a 5 × 5 × 3 monoclinic HfO_2 supercell was carried out by increasing the temperature up to 3300 K, corresponding to the melting point temperature of hafnia, and equilibrating the systems for 100 ps. To obtain statistically independent amorphous structures, we carried out the quench of the liquid every 5 ps decreasing the temperature to 1 K in 100 ps. During the entire process, the volume was allowed to change in the *z*-axis to maintain the pressure at 1 atm. Also, in the process, the cross section of amorphous samples (of ∼2.5 × 2.5 nm^2) is kept fixed to match the Hf electrodes, while the *z* relaxation gives to an initial dielectric thickness of approximately 1.5 nm.

Periodic boundary conditions (PBCs) were applied to the lateral dimensions. There is minimal crosstalk between filament instances, as the visualization of the filaments shows that their diameter is much smaller than the cell size, and typical diffusion lengths are also smaller than the cell size. These diffusion lengths can be estimated, for example, from Figure 5b). We see there that the radial MSD for the O atoms in the filament region at −2 V is ∼0.67 $Å^2$. Even in the worst possible scenario where all the MSD were attributed to the motion of a single vacancy, which would correspond to an in-plane displacement of ∼5.11 Å, this value is obtained by multiplying the average radial MSD of 0.67 $Å^2$ times the number of O atoms in the cylinder enclosing the filament, 39, and then taking the square root, which is below our lateral cell size, thus ensuring there are no spurious interactions between the PBC replicas of the simulation cells.

Filament Description. In order to characterize the formation and dissolution of the CF, it is necessary to identify and track the change in valence of the Hf atoms which can be done by following oxygen vacancies. In monoclinic hafnia ($mHfO_2$), vacancies are well-defined with respect to the perfect crystal structure,[33−35] since each atom has a specific atomic site, with a defined number of bonds, or coordination. In $aHfO_2$, this is not possible because there is no reference structure, and the Hf atoms have a distribution of possible coordination number, see Figure S2. To overcome this issue, we characterize changes in the dielectric and the formation of the CF during the operation of our cells, by computing the coordination of

https://doi.org/10.1021/acsnano.1c01466
ACS Nano 2021, 15, 12945−12954

Hf atoms (which determines their valence), instead of oxygen vacancies.

First-principles transport calculations have demonstrated quantized conductance in metal/mHfO_2/metal structures with single vacancy filaments,[36] resulting in Hf atoms bridging two oxygen vacancies (i.e., 5-fold coordinated hafnium). Therefore, we use the coordination number as the criterion to preform the CF analysis, defining as conductive those hafnium atoms with an oxygen coordination ≤5. Thus, in order to visualize the filament formation and disruption, we computed the oxygen coordination of all Hf atoms throughout the MD simulations using a cutoff for inclusion of 2.7 Å (corresponding to the minimum in the Hf−O radial distribution function; Figure S1). To find not-simply connected regions of high conductivity, we perform a cluster analysis between the Hf atoms with coordination ≤5, this enables us to determine the connectivity of the filament with the electrodes and the percolation of conductive states. The cluster analysis is carried out using a cutoff radius of 3.9 Å which corresponds to 30% of the bond order for two isolated Hf atoms.

Movies S1, S2, and S3 show the representative forming, reset, and set events.

Force Field and External Electrochemical Potential. All atomic interactions are described with a ReaxFF force field[37−39] parametrized for Hf−O systems, provided in the Supporting Information. As detailed in the Supporting Information, this force field reproduces some key structural parameters of aHfO_2, as well as the self-diffusion coefficient of oxygen, which at 500 K lies within a factor of 3 of the experimental value.[40] ReaxFF describes covalent interactions using partial bond orders and electrostatic interactions through environment-dependent partial atomic charges.[41] The atomic charges are calculated self-consistently according to the atomic structure, equaling the electrochemical potential of every atom in the system [electronegativity equalization method (EEM)].[42]

We simulate the effect of an external voltage to our MIM structures during forming, set, and reset via EChemDID.[19,43] This method describes an external electrochemical potential by adding an extra term to the electronegativity of metallic atoms in electrical contact with the electrodes. To apply a voltage Φ, we set the electronegativity of the atoms in the positive electrode to $\chi_0 - \Phi/2$ (with χ_0 a force field parameter), and those in the negative electrode to $\chi_0 + \Phi/2$. The electronegativity represents the local energy of electrons and is used to predict polarization and charge transfer via EEM. Prior work has shown that this approach results in a self-consistent description of electric fields and atomic changes.[19] The challenge is that in reactive simulations the atoms belonging to the electrode change with time; in our case, as conductive atoms become in contact with electrodes, the external potential needs to be applied to them. Thus, EChemDID assigns the desired constant external potential to a subset of atoms in both electrodes far away from the reactive interfaces and propagates and equilibrates the extra electrochemical potential through all atoms deemed metallic (i.e., Hf atoms with an oxygen coordination ≤ 5 as metallic ions). This is done via a nonphysical, but computationally efficient, diffusion equation:

$$\dot{\Phi} = k\nabla\Phi \tag{1}$$

where k is a diffusive constant. The details of this equilibration process are unimportant since the time scale of the relaxation of the electrochemical potential is much shorter than those of the atomic processes of interest. This equation is solved numerically on-the-fly during the MD simulations using atoms as a grid through the following expression:

$$\dot{\Phi}_i = k\sum_{k\neq i} \frac{\Phi_i(t) - \Phi_j(t)}{|R_{ij}|^2} w(R_{ij}) - \eta\, F(W_i)\, \Phi_i, \tag{2}$$

where η is a relaxation rate, $F(W)$ is a switching function that turns on when a metallic ion detaches from the other metallic atoms contacting the electrode, W_i is the total coordination of the atom i, and $w(R_{ij})$ is a weight function, calculated as

$$w(R_{ij}) = \begin{cases} N\left[1 - \left(\frac{R_{ij}}{R_C}\right)^2\right]^2 & \text{if } R_{ij} < R_C \\ 0 & \text{otherwise} \end{cases} \tag{3}$$

Here N is a normalization constant, and R_C is a cutoff radius below which two atoms are considered part of the same metallic cluster, and therefore, have the same electronegativity. The calculated potential Φ_i is then added to the atomic electronegativity of the metallic ions, $\chi_i(t) = \chi_0 + \Phi_i(t)$, used in charge equilibration to adjust the energy of valence electrons.

To solve EChemDID, the diffusion eq 2 was integrated 10 times per MD time step, while the atoms are maintained as fixed, using $k = 6$ Å^2/fs and $\eta = 0$. The parameters used in eq 3 were $R_C = 3.9$ Å and $N = 0.5$. Since the character of the atoms evolves during the reactive simulation, as conductive filaments form and break and the coordination of Hf atoms changes, the group of metallic ions over which EChemDID propagates the potential was updated every 50 ps. Updating the electronegativity as the simulations proceeded was necessary in order to obtain robust reset events, or set events at all. This stresses the importance of describing field enhancement and its 3D nature by tracking metallic atoms and their connectivity, which enables the application of accurate electrical boundary conditions crucial to the device operation. All the MD simulations have been carried out using the LAMMPS code,[44] with a time step of 0.2 fs.

REMARKS

The cycles we have presented all took place at the expected polarities for a bipolar device; no switching events were observed at the opposite polarity (e.g., reset for positive bias applied). However, a fraction of samples did not establish forming/switching under the corresponding bias, or it was unstable. This can be due to a number of causes. First, the small lateral dimensions of our simulated devices only lead to the presence of a single filament at a time; larger devices will have a higher chance of presenting a favorable region for filament formation, or the formation of multiple filaments (see section "Forming in larger samples" in the Supporting Information). Second, the forming step has only been allowed to run for 2.5 ns; the number of samples presenting filament formation might increase if forming had been allowed to run longer. Third, the thickness of our oxide, which is already quite small, is further lowered after the initial suboxide formation. A low oxide thickness favors successful forming; but on the other hand a longer filament in a thicker oxide might have several candidate spots for rupture, thus causing more robust reset events.

Finally, the effects of localized Joule heating (JH) are not included in our simulations (we do increase the temperature of the whole device to study the role of temperature in filament breakdown). JH would favor reset at high compliance currents, since atoms in the filament would have a higher diffusivity due to the increased temperature. Under a lower compliance current JH might favor the set as well, since a positive thermal feedback accelerating the set process is established in some cases,[45] or in large temperature gradients thermophoretic (Soret) forces may stabilize the conducting path against filament-breaking outward radial Fick diffusion,[21,46] although other authors did not observe this effect, and attributed filament breakup to the axial movement of the oxygen vacancies.[47]

https://doi.org/10.1021/acsnano.1c01466
ACS Nano 2021, 15, 12945−12954

ASSOCIATED CONTENT

Supporting Information

The Supporting Information is available free of charge at https://pubs.acs.org/doi/10.1021/acsnano.1c01466.

Structural parameters, diffusion coefficients calculations, stoichiometry profiles after interface relaxation, and tracking oxygen migration during forming, set, and reset (PDF)

ffield: ReaxFF file used in this work; param.qeq: force field parameters used for qeq scheme; reaxc_valence_angles.cpp.patch: File to patch the reaxc_valence_angles.cpp file in the USER-REAXC package; in.ahfo2: LAMMPS input file of a forming simulation, including EChemDID commands; mim-A-relaxed.data: atomic positions of a relaxed MIM structure (ZIP)

Movie S1: MD trajectory animation showing filament formation during forming (MPG)

Movie S2: MD trajectory animation showing a filament breakup event during reset (MPG)

Movie S3: MD trajectory animation showing a filament restoration event during set (MPG)

AUTHOR INFORMATION

Corresponding Authors

Xavier Cartoixà − *Departament d'Enginyeria Electrònica, Universitat Autònoma de Barcelona, 08193 Barcelona, Spain*; orcid.org/0000-0003-1905-5979; Email: Xavier.Cartoixa@uab.es

Alejandro Strachan − *School of Materials Engineering, Purdue University, West Lafayette, Indiana 47907, United States*; Email: strachan@purdue.edu

Authors

M. Laura Urquiza − *Departament d'Enginyeria Electrònica, Universitat Autònoma de Barcelona, 08193 Barcelona, Spain*

Md Mahbubul Islam − *Department of Mechanical Engineering, Wayne State University, Detroit, Michigan 48202, United States*; orcid.org/0000-0003-4584-2204

Adri C. T. van Duin − *Department of Mechanical Engineering, Pennsylvania State University, University Park, Pennsylvania 16802, United States*; orcid.org/0000-0002-3478-4945

Complete contact information is available at: https://pubs.acs.org/10.1021/acsnano.1c01466

Notes

The authors declare no competing financial interest.

ACKNOWLEDGMENTS

M.L.U. acknowledges the kind hospitality of the Birck Nanotechnology Center at Purdue University. M.L.U and X.C. acknowledge financial support by the Spanish Ministerio de Ciencia, Innovación y Universidades under Grant No. RTI2018-097876−B-C21 (MCIU/AEI/FEDER, UE). Computational support from nanoHUB and Purdue University is gratefully acknowledged.

REFERENCES

(1) Govoreanu, B.; Kar, G. S.; Chen, Y.; Paraschiv, V.; Kubicek, S.; Fantini, A.; Radu, I. P.; Goux, L.; Clima, S.; Degraeve, R. 10×10 nm^2 Hf/HfO_x Crossbar Resistive RAM with Excellent Performance, Reliability and Low-Energy Operation. *Int. Electron Devices Meet.* **2011**, 31.6.1−31.6.4.

(2) Lee, H. Y.; Chen, P. S.; Wu, T. Y.; Chen, Y. S.; Wang, C. C.; Tzeng, P. J.; Lin, C. H.; Chen, F.; Lien, C. H.; Tsai, M. Low Power and High Speed Bipolar Switching with a Thin Reactive Ti Buffer Layer in Robust HfO_2 Based RRAM. *Int. Electron Devices Meet.* **2008**, 1−4.

(3) Yang, Y. C.; Pan, F.; Liu, Q.; Liu, M.; Zeng, F. Fully Room-Temperature-Fabricated Nonvolatile Resistive Memory for Ultrafast and High-Density Memory Application. *Nano Lett.* **2009**, *9*, 1636−1643.

(4) Waser, R.; Dittmann, R.; Staikov, G.; Szot, K. Redox-Based Resistive Switching Memories − Nanoionic Mechanisms, Prospects, and Challenges. *Adv. Mater.* **2009**, *21*, 2632−2663.

(5) Menzel, S.; Böttger, U.; Wimmer, M.; Salinga, M. Physics of the Switching Kinetics in Resistive Memories. *Adv. Funct. Mater.* **2015**, *25*, 6306−6325.

(6) Pan, F.; Gao, S.; Chen, C.; Song, C.; Zeng, F. Recent Progress in Resistive Random Access Memories: Materials, Switching Mechanisms, and Performance. *Mater. Sci. Eng., R* **2014**, *83*, 1−59.

(7) Celano, U.; Goux, L.; Belmonte, A.; Opsomer, K.; Franquet, A.; Schulze, A.; Detavernier, C.; Richard, O.; Bender, H.; Jurczak, M.; Vandervorst, W. Three-Dimensional Observation of the Conductive Filament in Nanoscaled Resistive Memory Devices. *Nano Lett.* **2014**, *14*, 2401−2406.

(8) Fergus, J. W. Electrolytes for Solid Oxide Fuel Cells. *J. Power Sources* **2006**, *162*, 30−40.

(9) Tesfai, A.; Irvine, J. Solid Oxide Fuel Cells: Theory and Materials. *Comprehensive Renewable Energy* **2012**, *4*, 261−276.

(10) Xue, K.-H.; Blaise, P.; Fonseca, L. R. C.; Nishi, Y. Prediction of Semimetallic Tetragonal Hf_2O_3 and Zr_2O_3 from First Principles. *Phys. Rev. Lett.* **2013**, *110*, 065502.

(11) Celano, U.; Goux, L.; Degraeve, R.; Fantini, A.; Richard, O.; Bender, H.; Jurczak, M.; Vandervorst, W. Imaging the Three-Dimensional Conductive Channel in Filamentary-Based Oxide Resistive Switching Memory. *Nano Lett.* **2015**, *15*, 7970−7975.

(12) Privitera, S.; Bersuker, G.; Butcher, B.; Kalantarian, A.; Lombardo, S.; Bongiorno, C.; Geer, R.; Gilmer, D.; Kirsch, P. Microscopy Study of the Conductive Filament in HfO_2 Resistive Switching Memory Devices. *Microelectron. Eng.* **2013**, *109*, 75−78.

(13) Traoré, B.; Blaise, P.; Vianello, E.; Perniola, L.; De Salvo, B.; Nishi, Y. HfO_2-Based RRAM: Electrode Effects, Ti/HfO_2 Interface, Charge Injection, and Oxygen (O) Defects Diffusion through Experiment and *ab Initio* Calculations. *IEEE Trans. Electron Devices* **2016**, *63*, 360−368.

(14) Kindsmüller, A.; Meledin, A.; Mayer, J.; Waser, R.; Wouters, D. J. On the Role of the Metal Oxide/Reactive Electrode Interface during the Forming Procedure of Valence Change ReRAM Devices. *Nanoscale* **2019**, *11*, 18201−18208.

(15) He, W.; Sun, H.; Zhou, Y.; Lu, K.; Xue, K.; Miao, X. Customized Binary and Multi-Level HfO_{2-x}-Based Memristors Tuned by Oxidation Conditions. *Sci. Rep.* **2017**, *7*, 10070.

(16) Chen, Y. Y.; Goux, L.; Clima, S.; Govoreanu, B.; Degraeve, R.; Kar, G. S.; Fantini, A.; Groeseneken, G.; Wouters, D. J.; Jurczak, M. Endurance/Retention Trade-Off on HfO_2/Metal Cap 1T1R Bipolar RRAM. IEEE Trans. *IEEE Trans. Electron Devices* **2013**, *60*, 1114−1121.

(17) Park, G.-S.; Kim, Y. B.; Park, S. Y.; Li, X. S.; Heo, S.; Lee, M.-J.; Chang, M.; Kwon, J. H.; Kim, M.; Chung, U.-I.; Dittmann, R.; Waser, R.; Kim, K. *In Situ* Observation of Filamentary Conducting Channels in an Asymmetric Ta_2O_{5-x}/TaO_{2-x} Bilayer Structure. *Nat. Commun.* **2013**, *4*, 2382.

(18) Hur, J. H.; Lee, M.-J.; Lee, C. B.; Kim, Y.-B.; Kim, C.-J. Modeling for Bipolar Resistive Memory Switching in Transition-Metal Oxides. *Phys. Rev. B: Condens. Matter Mater. Phys.* **2010**, *82*, 155321.

(19) Onofrio, N.; Strachan, A. Voltage Equilibration for Reactive Atomistic Simulations of Electrochemical Processes. *J. Chem. Phys.* **2015**, *143*, 054109.

(20) Onofrio, N.; Guzman, D.; Strachan, A. Atomic Origin of Ultrafast Resistance Switching in Nanoscale Electrometallization Cells. *Nat. Mater.* **2015**, *14*, 440−446.
(21) Strukov, D. B.; Alibart, F.; Williams, R. S. Thermophoresis/Diffusion as a Plausible Mechanism for Unipolar Resistive Switching in Metal−Oxide−Metal Memristors. *Appl. Phys. A: Mater. Sci. Process.* **2012**, *107*, 509−518.
(22) Humphrey, W.; Dalke, A.; Schulten, K. VMD: Visual Molecular Dynamics. *J. Mol. Graphics* **1996**, *14*, 33−38.
(23) Stone, J. An Efficient Library for Parallel Ray Tracing and Animation. M.Sc. thesis, University of Missouri-Rolla, Rolla, MO, 1998.
(24) Sharath, S. U.; Bertaud, T.; Kurian, J.; Hildebrandt, E.; Walczyk, C.; Calka, P.; Zaumseil, P.; Sowinska, M.; Walczyk, D.; Gloskovskii, A.; Schroeder, T.; Alff, L. Towards Forming-Free Resistive Switching in Oxygen Engineered HfO_{2-x}. *Appl. Phys. Lett.* **2014**, *104*, 063502.
(25) Sowinska, M.; Bertaud, T.; Walczyk, D.; Thiess, S.; Schubert, M. A.; Lukosius, M.; Drube, W.; Walczyk, C.; Schroeder, T. Hard X-Ray Photoelectron Spectroscopy Study of the Electroforming in Ti/HfO_2-Based Resistive Switching Structures. *Appl. Phys. Lett.* **2012**, *100*, 233509.
(26) O'Hara, A.; Bersuker, G.; Demkov, A. A. Assessing Hafnium on Hafnia as an Oxygen Getter. *J. Appl. Phys.* **2014**, *115*, 183703.
(27) Nosé, S. A. Unified Formulation of the Constant Temperature Molecular Dynamics Methods. *J. Chem. Phys.* **1984**, *81*, 511−519.
(28) Hoover, W. G. Canonical Dynamics: Equilibrium Phase-Space Distributions. *Phys. Rev. A: At., Mol., Opt. Phys.* **1985**, *31*, 1695−1697.
(29) Long, S.; Lian, X.; Cagli, C.; Cartoixà, X.; Rurali, R.; Miranda, E.; Jiménez, D.; Perniola, L.; Liu, M.; Suñé, J. Quantum-Size Effects in Hafnium-Oxide Resistive Switching. *Appl. Phys. Lett.* **2013**, *102*, 183505.
(30) Menzel, S.; Waser, R. In *Advances in Non-Volatile Memory and Storage Technology*, 2nd ed.; Magyari-Köpe, B., Nishi, Y., Eds.; Woodhead Publishing Series in Electronic and Optical Materials; Woodhead Publishing: Duxford, U.K., 2019; pp 137−170.
(31) Schie, M.; Menzel, S.; Robertson, J.; Waser, R.; De Souza, R. A. Field-Enhanced Route to Generating Anti-Frenkel Pairs in HfO_2. *Phys. Rev. Mater.* **2018**, *2*, 035002.
(32) Jeong, D. S.; Schroeder, H.; Waser, R. Coexistence of Bipolar and Unipolar Resistive Switching Behaviors in a Pt/TiO_2/Pt Stack. *Electrochem. Solid-State Lett.* **2007**, *10*, G51.
(33) Bradley, S. R.; Shluger, A. L.; Bersuker, G. Electron-Injection-Assisted Generation of Oxygen Vacancies in Monoclinic HfO_2. *Phys. Rev. Appl.* **2015**, *4*, 064008.
(34) Foster, A. S.; Lopez Gejo, F.; Shluger, A. L.; Nieminen, R. M. Vacancy and Interstitial Defects in Hafnia. *Phys. Rev. B: Condens. Matter Mater. Phys.* **2002**, *65*, 174117.
(35) Zheng, J. X.; Ceder, G.; Maxisch, T.; Chim, W. K.; Choi, W. K. First-Principles Study of Native Point Defects in Hafnia and Zirconia. *Phys. Rev. B: Condens. Matter Mater. Phys.* **2007**, *75*, 104112.
(36) Cartoixà, X.; Rurali, R.; Suñé, J. Transport Properties of Oxygen Vacancy Filaments in Metal/Crystalline or Amorphous HfO_2/Metal Structures. *Phys. Rev. B: Condens. Matter Mater. Phys.* **2012**, *86*, 165445.
(37) Senftle, T. P.; Hong, S.; Islam, M. M.; Kylasa, S. B.; Zheng, Y.; Shin, Y. K.; Junkermeier, C.; Engel-Herbert, R.; Janik, M. J.; Aktulga, H. M.; et al. The ReaxFF Reactive Force-Field: Development, Applications and Future Directions. *npj Comput. Mater.* **2016**, *2*, 15011.
(38) van Duin, A. C. T.; Dasgupta, S.; Lorant, F.; Goddard, W. A. ReaxFF: A Reactive Force Field for Hydrocarbons. *J. Phys. Chem. A* **2001**, *105*, 9396−9409.
(39) Aktulga, H.; Fogarty, J.; Pandit, S.; Grama, A. Parallel Reactive Molecular Dynamics: Numerical Methods and Algorithmic Techniques. *Parall. Comput.* **2012**, *38*, 245−259.
(40) Zafar, S.; Jagannathan, H.; Edge, L. F.; Gupta, D. Measurement of Oxygen Diffusion in Nanometer Scale HfO_2 Gate Dielectric Films. *Appl. Phys. Lett.* **2011**, *98*, 152903.
(41) Rappe, A. K.; Goddard, W. A. Charge Equilibration for Molecular Dynamics Simulations. *J. Phys. Chem.* **1991**, *95*, 3358−3363.
(42) Mortier, W. J.; Ghosh, S. K.; Shankar, S. Electronegativity-Equalization Method for the Calculation of Atomic Charges in Molecules. *J. Am. Chem. Soc.* **1986**, *108*, 4315−4320.
(43) EChemDID and various USER packages for LAMMPS. https://github.com/nonofrio/LAMMPS-hacks-public (accessed on June 3, 2021).
(44) Plimpton, S. Fast Parallel Algorithms for Short-Range Molecular Dynamics. *J. Comput. Phys.* **1995**, *117*, 1−19.
(45) Fleck, K.; La Torre, C.; Aslam, N.; Hoffmann-Eifert, S.; Böttger, U.; Menzel, S. Uniting Gradual and Abrupt Set Processes in Resistive Switching Oxides. *Phys. Rev. Appl.* **2016**, *6*, 064015.
(46) Kumar, S.; Wang, Z.; Huang, X.; Kumari, N.; Davila, N.; Strachan, J. P.; Vine, D.; Kilcoyne, A. L. D.; Nishi, Y.; Williams, R. S. Conduction Channel Formation and Dissolution Due to Oxygen Thermophoresis/Diffusion in Hafnium Oxide Memristors. *ACS Nano* **2016**, *10*, 11205−11210.
(47) Marchewka, A.; Roesgen, B.; Skaja, K.; Du, H.; Jia, C.-L.; Mayer, J.; Rana, V.; Waser, R.; Menzel, S. Nanoionic Resistive Switching Memories: On the Physical Nature of the Dynamic Reset Process. *Adv. Electron. Mater.* **2016**, *2*, 1500233.

https://doi.org/10.1021/acsnano.1c01466
ACS Nano 2021, 15, 12945−12954